J Mater Sci: Mater Med (2010) 21:189–206
DOI 10.1007/s10856-009-3858-2

The mesoporosity of microparticles spray dried from trehalose and nanoparticle hydroxyapatite depends on the ratio of nanoparticles to sugar and nanoparticle surface charge

David M. Wright · Zlatko S. Saracevic · Nigel H. Kyle · Michael Motskin · Jeremy N. Skepper

Received: 10 July 2009 / Accepted: 13 August 2009 / Published online: 29 August 2009

Abstract The ratio of hydroxyapatite (HA) nanoparticles (NP) to trehalose in composite microparticle (MP) vaccine vehicles by determining inter-nanoparticle space potentially influences antigen release. Mercury porosimetry and gas adsorption analysis have been used quantify this space. Larger pores are present in MPs spray dried solely from nanoparticle gel compared with MPs spray dried from nanoparticle colloid which have less inter-nanoparticle volume. This is attributed to tighter nanoparticle packing caused by citrate modification of their surface charge. The pore size distributions (PSD) for MP where the trehalose has been eliminated by combustion generally broaden and shifts to higher values with increasing initial trehalose content. Modal pore size, for gel derived MPs is comparable to modal NP width below 30% initial trehalose content and approximates to modal NP length ($\sim$50 nm) at 60% initial trehalose content. For colloidally derived MPs this never exceeds the modal NP width. Pore-sizes are comparable, to surface inter-nanoparticle spacings observed by SEM.

D. M. Wright (✉) · M. Motskin · J. N. Skepper
Department of Physiology, Development and Neuroscience, Multi-Imaging Centre School of Biological Sciences, Anatomy Building, Downing Street, Cambridge CB2 3DY, UK
e-mail: dmw31@cam.ac.uk

Z. S. Saracevic
Department of Chemical Engineering and Biotechnology, University of Cambridge, New Museums Site, Pembroke Street, Cambridge CB2 3RA, UK

N. H. Kyle
Cambridge Biostability Ltd., Unit 184, Cambridge Science Park, Milton Road, Cambridge, Cambridgeshire CB4 0GA, UK

1 Introduction

Microparticles (MP) consisting of hundreds of thousands of lozenge shaped, single crystal hydroxyapatite nanoparticles (NP), approximately 14 nm wide and 60 nm long, vitrified in a sugar-glass or amino-glass matrix are currently under development as a sustained delivery system for vaccines [1, 2]. The sugar glass phase stabilises protein antigens for storage, without refrigeration, in a non-aqueous delivery fluid. The NP component that was initially added to make the MPs neutrally buoyant in the carrier liquid may also prolong antigen release.

Altering the sugar-nanoparticle ratio may affect the division of inter-nanoparticle space and in turn influence the time scale over which antigen escapes the confines of the MP or the rate at which physiological fluids penetrate the MP's interior. In an acid environment, the latter will determine how quickly MPs fragment and eventually disintegrate, through the dissolution of inter-nanoparticle linkages formed during drying, into their component NPs exposing the surface bound antigen. Such disintegration has been observed for MPs spray dried from hydroxyapatite (HA) NPs alone when taken up in vitro by human monocyte macrophages [1] and will occur in vivo prolonging release.

MPs with large fractions of sugar do not infiltrate with epoxy resin and cannot be sectioned by ultramicrotomy. Focused ion beam (FIB) milling has therefore been used as a means of creating ultra thin foils for ultrastructural examination [2]. The time consuming nature of this technique does not permit the inspection of the large numbers of MPs required to determine the space between NPs by stereology. Current dual beam microscopes mill too coarsely, with a minimum slice thickness >5 nm, to three dimensionally render MPs internal volume. X-ray tomograms can be

produced using a synchrotron source with sub-100-nm resolution [3] although even in 2D the spatial resolution of current x-ray microscopes, around 15 nm, is also too coarse to determine pore size distributions within spray dried HA MPs. Electron-tomography techniques, successfully applied to the study of catalysts [3] are becoming less protracted. These could potentially be used to statistically sample inter-nanoparticle space but still remain too costly for comparison of a large number of preparations.

Alternative methods must therefore, be employed to quantify the inter-nanoparticle space for preparations with different fractions of sugar to allow their comparison. The approach attempted here is to eliminate the glass sugar component by combustion and quantify the inter-nanoparticle space with the complimentary techniques of mercury porosimetry and gas adsorption analysis [4].

Mercury porosimetry measures the volume of liquid mercury forced into the pore space as the pressure is increased. Mercury does not wet most substances and is therefore used as it cannot fill pores by capillary action. It is possible to determine the pore size distribution (PSD) by assuming a material is composed of pores of cylindrical crossection composed and relating the applied pressure (P) to the diameter of the pores (D) using the Washburn equation $DP = -4\gamma Cos(\theta)$ [5] where γ the surface tension of mercury (480 dyne cm^{-1}) and θ the contact angle between pore wall and mercury($\sim 140°$). It has been widely used to study porosity of materials classified mesoporous (2 nm $<$ w$<$50 nm) and macroporous ($w > 50$ nm) by IUPAC [6] including, cements [7], tissue replacement, scaffolds [8, 9] adsorbents and catalysts [10]. Mercury porosimetry can measure pores sizes exceeding 400 μm in diameter but is not used to study materials classified as microporous as the smallest pore size it can measure which is limited by the maximum pressure obtainable by the porosimeter, is about 2 nm in diameter [11].

A gas analyser generates isotherms by measuring the amount (volume) of gas, most often nitrogen (N_2), adsorbed by or desorbed from a material held at a constant temperature which is usually that of liquid nitrogen, as pressure is raised or lowered [11]. By modelling these isotherms information about a samples surface area and porosity can be derived. As pressure is increased from vacuum gas molecules increasingly populate the surface of a material until a liquid monolayer forms. In this regime Brunauer–Emmett–Teller (BET) [12] analysis can be used to determine the total internal surface area of a material from the isotherm by equating the rate gas molecule condensation onto an absorbed layer to the rate of evaporation from that layer and summing over an infinite number of layers. T plot analysis can also be used in this regime to determine the amount of micropores (pores $<$2 nm in diameter) pressure. Further increases in pressure towards ambient thickens the adsorbed layer filling progressively larger pores until the bulk of the material is filled. The Barrett, Joyner and Halenda (BJH method) [13] determines detailed pore information by modelling the stepwise emptying of the condensed absorptive from pores of a specific chosen geometry as pressure is decreased to fit the isotherm. The upper limit of pore size determine by this technique is 200 nm. The lower limit of BJH method is about 2 nm as the Kelvin equation used in BJH analysis neglects the build-up of adsorbed layers on pore walls prior to condensation, and because the gas and liquid in small mesopores and micropores cannot be treated as uniform phases separated by an interface [14].

Both techniques have limitations and make assumptions about the internal organization of a material in order to determine the pore size distribution but when used in conjunction with microscopy they should allow detailed comparison of materials with differing porosities.

2 Methods

2.1 Materials

HA NP were prepared, after the method of Kumta et al. [15], by adding 2 l of 150 mM calcium chloride ($CaCl_2{\cdot}2H_2O$, Sigma-Aldrich) to 2 l 100 mM trisodium orthophosphate dodecahydrate ($Na_3PO_4{\cdot}12H_2O$, Sigma-Aldrich) and stirring thoroughly in an ultrasonic bath (FS200, Decon, UK) for 1 h at ambient temperature. NP suspensions were then washed thoroughly in deionised water and sterilised by autoclaving at 121°C for 15 min in an autoclave (Vario 19, Dixons, UK). Colloidal suspensions of HA NPs were prepared by adding sufficient sodium citrate to the gel suspension to obtain a 200 mM concentration. The citrate containing suspension was stirred at ambient temperature for 30 min, then transferred into dialysis tubing and dialysed against a large excess of deionised water for at least 24 h to remove the excess sodium citrate. Both gel and colloidal nanoparticle suspensions were stored at 4°C prior to use.

After washing and sterilization the concentration of nanoparticles was adjusted to 30 mg/ml.

To produce microparticles without sugar, this suspension was used directly as the feedstock to the spray dryer. Trehalose was added to the NP suspension at a ratio of x:1 − x w/w, where x is the trehalose fraction, and the concentration was adjusted to 30 mg/ml (total solids added) as the feedstock for producing MP with 100 × x% sugar. The feedstock was maintained in moderate agitation by a magnetic stirrer (Ikamag, USA) and fed into the spray dryer using a built-in peristaltic pump with a feed flow rate of 2.5 ml/min and was spray dried using a Buchi B290

Advanced Spray Dryer (Flawil, Switzerland). The dryer was equipped with a 0.7 mm diameter nozzle and was operated with an air outlet temperature of 100°C. The atomizing air gauge was set to 50 from a 6 bar source. The aspirator was set to 100%. Spray dried samples were transferred directly from the spray drier to vials in a purpose made desiccator maintained below 3% RH.

2.2 Trehalose combustion

MPs were heated to 500°C at a rate of 5°C/min in covered alumina crucibles inside an ashing furnace (Carbolite). Samples were held at that temperature for 5 h then allowed to cool to ambient. Each sample was weighed before and after heating to confirm the weight loss due to combustion of the sugar. Thermal gravitational analysis (TGA) was used to confirm that no further weight loss occurred after heating above 500°C. Representative samples were heated for a subsequent 5 h to confirm that no further weight loss occurred. Samples were then stored in sealed glass vials at 60°C until analysis.

2.3 Gas analysis

Nitrogen absorption and desorbtion isotherms were obtained and analysed using a gas analyser, TriStar 3000. The Brunauer–Emmett–Teller (BET) method was used to determine the total internal surface area from the isotherm. Micropore area was determined by T plot analysis by using the Halsey model to model the thickness of the adsorbed layer. Pore size distributions were determined from isotherms by Barrett, Joyner and Halenda (BJH) analysis.

2.4 Mercury porosimetry

Mercury intrusion isotherms obtained using a mercury poresimeter (Micromeritics AutoPore IV) using an evacuation pressure of 50 μmHg, an evacuation time of 5 min, a filling pressure of 0.95 psia and an equilibration time of 80 s. Pore size distributions were obtained by plotting the log differential intrusion against the pore size calculated from the pressure using the Washburn equation.

2.5 Skeletal density measurement

The skeletal density of powders was determined using a helium pycometer (Micromeritics Accupyc1330) using $\sim$1 cm^3 of powder.

2.6 Electron microscopy

For scanning electron microscopy microparticles, were dispersed on the surface of an aluminium Cambridge SEM stub and sputter coated with a 4 nm layer of gold (Quorum EmiTech, K575X) and viewed in a FEI XL30 SEM operated at 5 KeV.

2.7 Transmission electron microscopy

TEM imaging of nanoparticles was performed on material deposited by drying droplets of (1–5 mg/l) colloidal or gel suspensions diluted in DIW on 400 mesh, holey carbon, film grids (Agar Scientific).

3 Results

NPs, supplied as either gel or colloidal suspension to the spray drier consist of lozenge shaped NPs, Fig. 1a. Their length, Fig. 1b, ranges from 10 to 100 nm with a mean of 50 ± 19 nm (SD) and their width, Fig. 1d, ranges from 8 to 40 nm with a mean of 18 ± 5 nm (SD). NP aspect ratio ranges from 1 to 5, Fig. 1c with a mean of 2.90 ± 1.24 (SD). Powder X-ray diffraction, Fig. 2, confirms that NPs are phase pure HA.

TGA, Fig. 3, shows that little weight change is observed after heating microparticles with varying amounts of sugar above 500°C in air. Heating at 500°C in air produced no further changes in MP weight after 3 h. The density of MPs obtained by helium pycnometry (3.01 ± 0.1 cm^3/g) on material spray dried with a significant fraction of trehalose spray dried (55% colloid − 45% trehalose) after combustion was indistinguishable from that obtained for material spray dried without trehalose.

3.1 Porosity of material spray dried from 100% hydroxyapatite prior to heat treatment

Figure 4 shows the cumulative mercury intrusion–extrusion curves for microparticle material spray dried from 100% HA gel, curve a and colloid, curve b, before heat treatment at 500°C. These curves have a hysteresis loop, below 1000 psia, caused by the infiltration of mercury between MPs and a hysteresis loop, above 1000 psia, due to the infiltration of mercury between NPs. Inter-nanoparticle volume, pore volume, was determined by subtracting the 1000 psia from the cumulative intrusion at 30000 psia. Corresponding N_2 gas isotherms for spray dried gel, curve a Fig. 5, and spray dried colloid, curve b Fig. 5 are type IV isotherms indicative of meso-porous materials. The initial slope of these curves suggests little microporosity. Spray dried gel has measurable microporosity, Table 1, representing about 10% of the total surface area but only 1% of total pore volume. Spray dried colloid has negligible microporosity unquantifiable using the halsey film thickness for T-plot analysis. BJH analysis and mercury porosimetry provide comparable

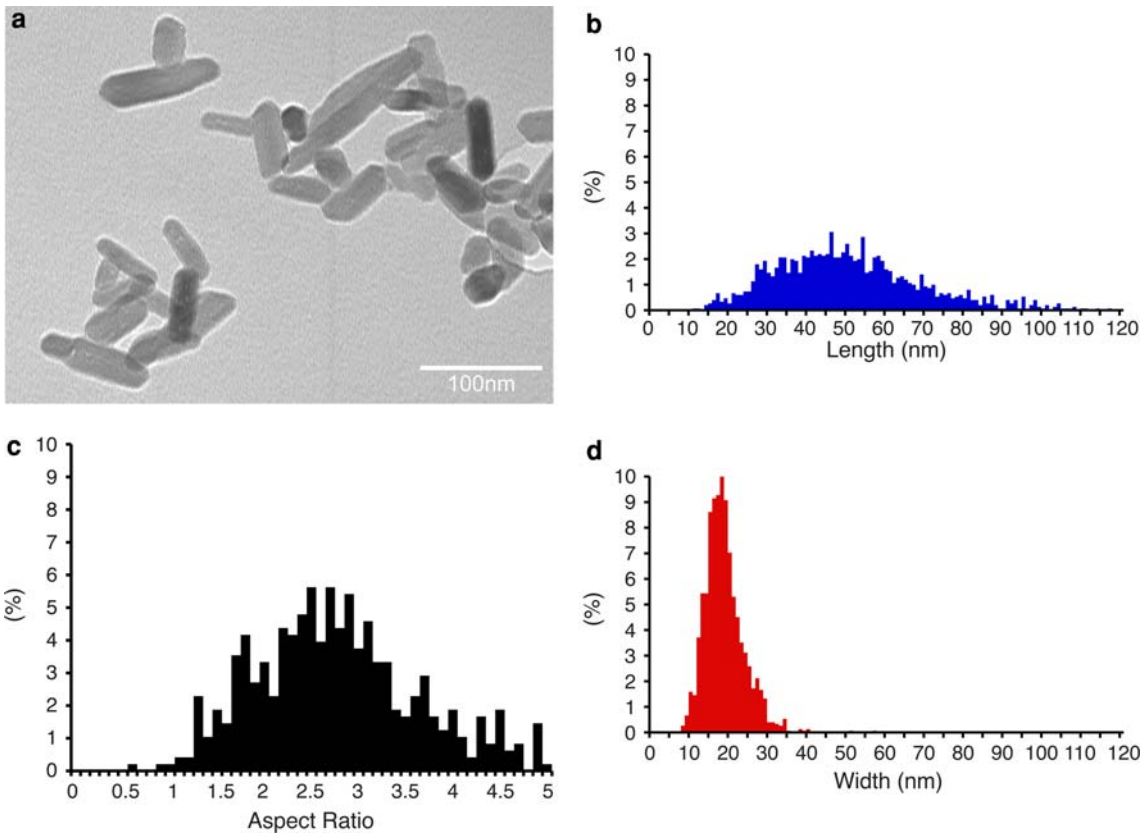

Fig. 1 Feedstock of hydroxyapatite nanoparticles used for spray drying. **a** TEM image, **b** length distribution, **c** aspect ratio distribution, **d** width distribution

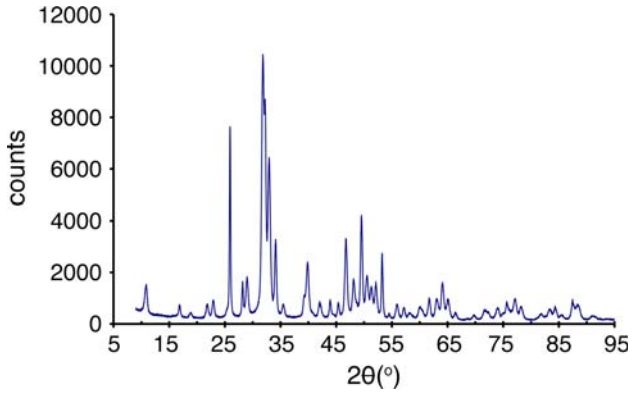

Fig. 2 Powder X ray diffraction trace for feed stock to the spray drier

measurements of pore volume. Spray dried gel has 25% greater pore volume than spray dried colloid.

PSDs obtained by mercury porosimetry on spray dried material before heat treatment are negatively skewed. Spray dried colloid before heat treatment, Fig. 6 curve a, has a narrow distribution of pores ranging from 5 to 18 nm diameter with a modal diameter of 12 nm. Spray dried gel,

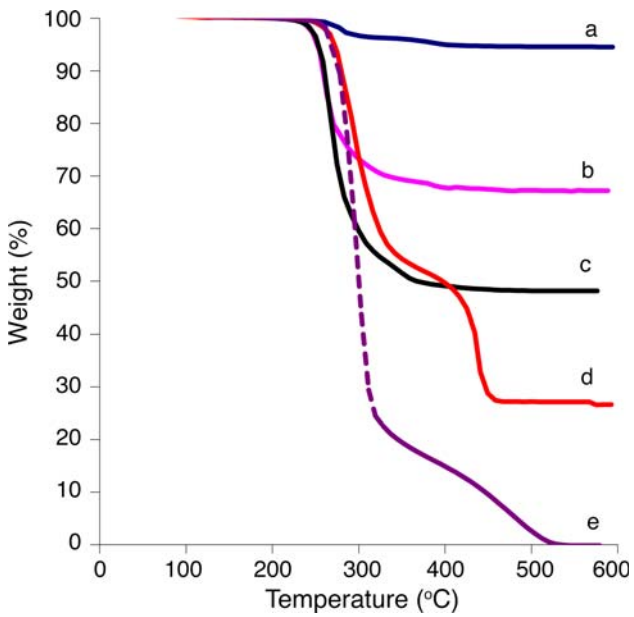

Fig. 3 Thermal gravitational analysis of MPs spray dried from (*a*) 100% NPs, (*b*) 70% NPs-30% trehalose, (*c*) 50% trehalose-50% NPsm, (*d*) 30% NPs-70% trehalose and (*e*) 100% trehalose

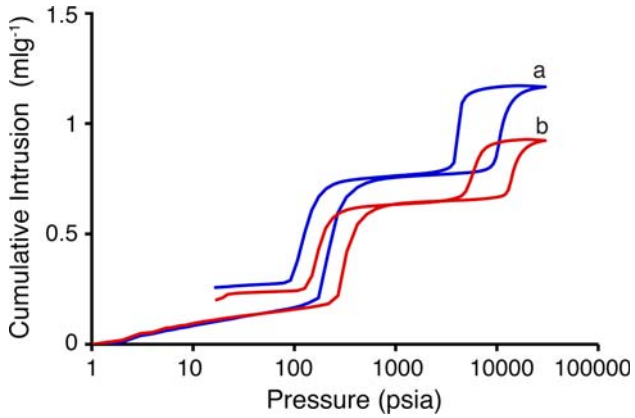

Fig. 4 Cumulative mercury intrusion–extrusion for MPs spray dried from (*a*) colloid and (*b*) gel without heating

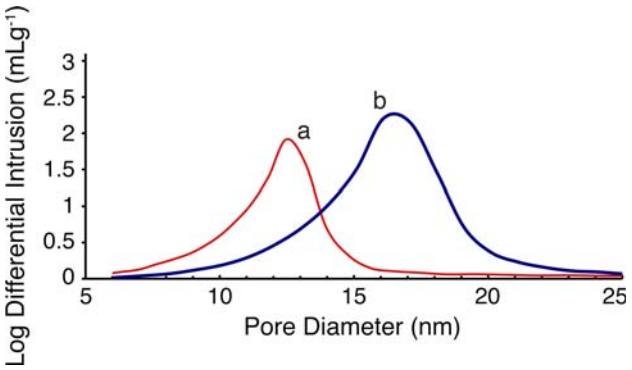

Fig. 6 Pore size distribution obtained by mercury intrusion for material spray dried from 100% HA colloid (*a*) prior to heat treatment and (*b*) after heating to 500°C for 3 h

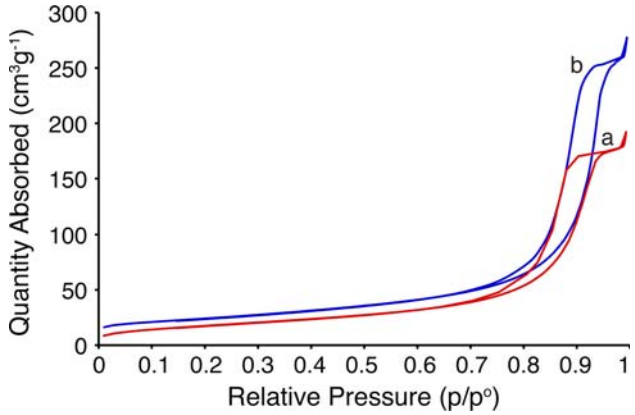

Fig. 5 Nitrogen gas adsorption–desorption isotherm for MPs spray dried from (*a*) colloid and (*b*) gel without heating

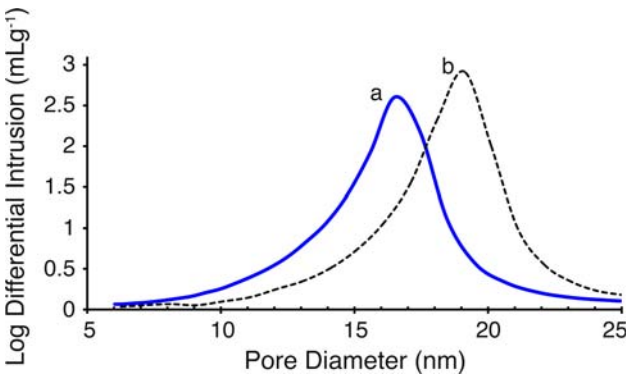

Fig. 7 Pore size distribution obtained by mercury intrusion for material spray dried from 100% HA gel (*a*) prior to heat treatment and (*b*) after heating to 500°C for 3 h

curve a Fig. 7 has larger mesopores ranging from 6 and 30 nm in diameter with a mode of 16.8 nm.

BJH analysis of desorption branch of the gas isotherm generates slightly larger pore sizes and more symmetrical distributions than analysis of mercury intrusion. According to this method, for spray dried colloid (Fig. 8 curve a) pores range from 5 to 25 nm in diameter with a mode of 15 nm and for spray dried gel (Fig. 9 curve a) pores range from 5 to 35 nm peak with a mode of 18 nm. In comparison to BJH analysis of desorption, larger pore sizes with wider, more skewed pore distributions are generated by BJH analysis of adsorption, Table 2. Analysis of adsorption, for spray dried colloid, curve b Fig. 8, generates pore diameters ranging from 2 to over 42 nm with a peak at 21 nm. For spray dried gel, curve b Fig. 9, the pore size distribution extends from 2 to 60 nm with a mode of 32 nm.

3.2 Porosity of material spray dried from 100% hydroxyapatite after heat treatment

Heating material spray dried solely from HA NPs to 500°C results in narrower, less skewed pore size distributions

Table 1 Pore volume and pore area parameters obtained spray dried gel and spray dried colloid material before heat treatment determined by BJH analysis and Mercury Porosimetry

Preparation	Micropore area ($m^2\ g^{-1}$)	Micropore area (%)	External surface area ($m^2\ g^{-1}$)	Total surface area (BET) ($m^2\ g^{-1}$)	Micropore volume ($\times 10^{-3}\ cm^3\ g^{-1}$)	Micropore volume (%)	Cumulative pore volume (BJH) ($cm^3\ g^{-1}$)	Pore volume (Mercury) ($cm^3\ g^{-1}$)	Total pore area (Mercury) ($m^2\ g^{-1}$)
Gel	10.4 ± 0.7	11.0 ± 0.8	84.4 ± 0.8	94.9 ± 1.5	4.7 ± 0.2	1.17 ± 0.05	0.40 ± 0.01	0.39 ± 0.01	110.0 ± 1.73
Colloid	*	*	*	61.6 ± 2.9	*	*	0.29 ± 0.02	0.27 ± 0.02	87.5 ± 8.2

* Cannot be determined by T-plot analysis

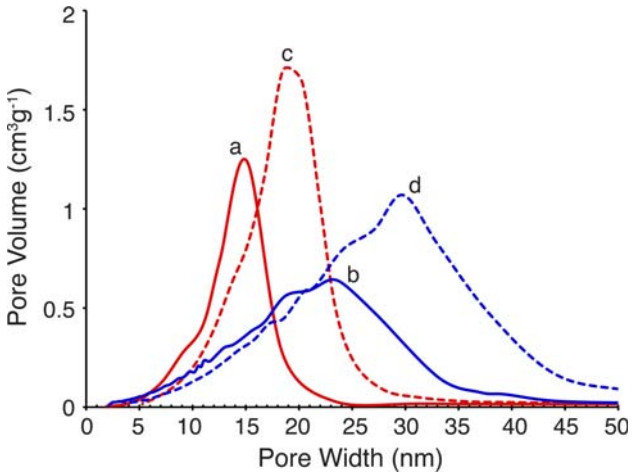

Fig. 8 Pore size distributions obtained by BJH analysis of MPs spray dried from 100% colloidal HA NP suspension (*a*) desorption branch prior to heating, (*b*) adsorption branch prior to heating, (*c*) desorption branch after heating to 500°C for 3 h and (*d*) adsorption branch after heating 500°C for 3 h

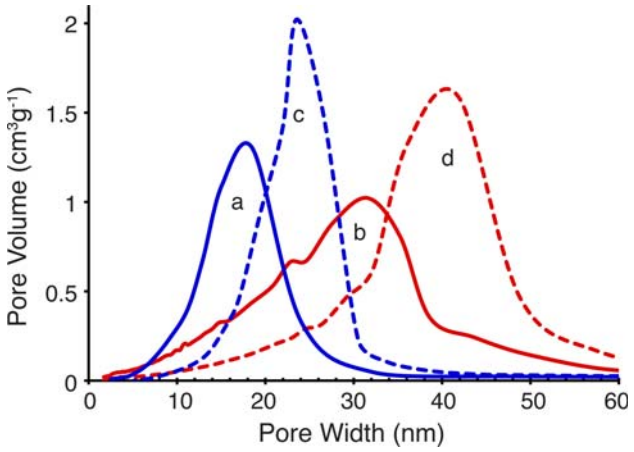

Fig. 9 Pore size distributions obtained by BJH analysis of MPs spray dried from 100% colloidal HA NP gel (*a*) desorption branch prior to heating, (*b*) adsorption branch prior to heating, (*c*) desorption branch after heating to 500°C for 3 h and (*d*) adsorption branch

shifted to larger values along the X-ordinate according to both BJH analysis and mercury porosimetry.

According mercury porosimetry measurement, heat treatment of spray dried colloid (Fig. 6 curve b) increases the modal pore size to 16.5 nm and maximum pore size to 25 nm. BJH analysis of N_2 desorption, shows a similar shift when heating this material. Comparing of curve a for unheated material and curve c, for heat treated material, in Fig. 8 modal pore size increases from 15 to 19 nm and maximum pore size increases from 25 to 35 nm at the expense of pores below 10 nm.

Comparing curves a and b in Fig. 7 for mercury porosimetry measurement of spray dried gel before and after heat treatment, it can be seen that heat treatment centres the pore distribution about a higher modal value of 20 nm and that porosity is gained between 20 and 24 nm but lost below 8 nm. Comparing curves a and c Fig. in 8 obtained by BJH analysis of N_2 desorption before and after heat treatment on the same material, shows that the modal pore size increases to 24 nm and porosity gained between 30 and 35 nm but lost below 8 nm.

A 24% increase in the inter-nanoparticle space from 0.39 to 0.48 ml g^{-1} was observed using BJH analysis due to heating spray dried colloid (from the same batch). Whereas, a 20% increase in inter-nanoparticle space to 0.35 ml g^{-1} occurs as a result of heat treatment of spray dried colloid according mercury porosimetry. For spray dried gel mercury porosimetry suggest a 7% reduction in internanoparticle space from 0.41 to 0.38 ml g^{-1} after heating whereas, BJH analysis indicates no change in pore volume. SEM images for MPs spray dried without trehalose before and after heat treatment are shown in Fig. 10. The packing of NPs at surface of MPs spray dried from HA gel appears unchanged by heat treatment. Whereas, NPs on the surface of MPs spray dried from colloidal HA appear to be loosened slightly by heat treatment.

Table 2 Parameters ascribed to the pore size distributions obtained Mercury Porosimetry and BJH analysis of the desorption and adsorption for microparticles spray dried from 100% hydroxyapatite before heat treatment

Preparation (%)	Method of measurement	Figure and curve	Minimum (nm)	Maximum (nm)	Range (nm)	Peak (nm)	Width at half height (nm)	Peak Height (cm^3 g^{-1})
Gel	Mercury	7a	6	30	24	16.8	4	2.60
	BJH Desorption	9a	5	36	31	18	9	1.35
	BJH Adsorption	9b	2	60	58	31	18	1.05
Colloid	Mercury	6a	6	20	14	13	3	1.80
	BJH Desorption	8a	5	26	21	15	5	1.33
	BJH Adsorption	8b	2	50	48	23	18	0.64

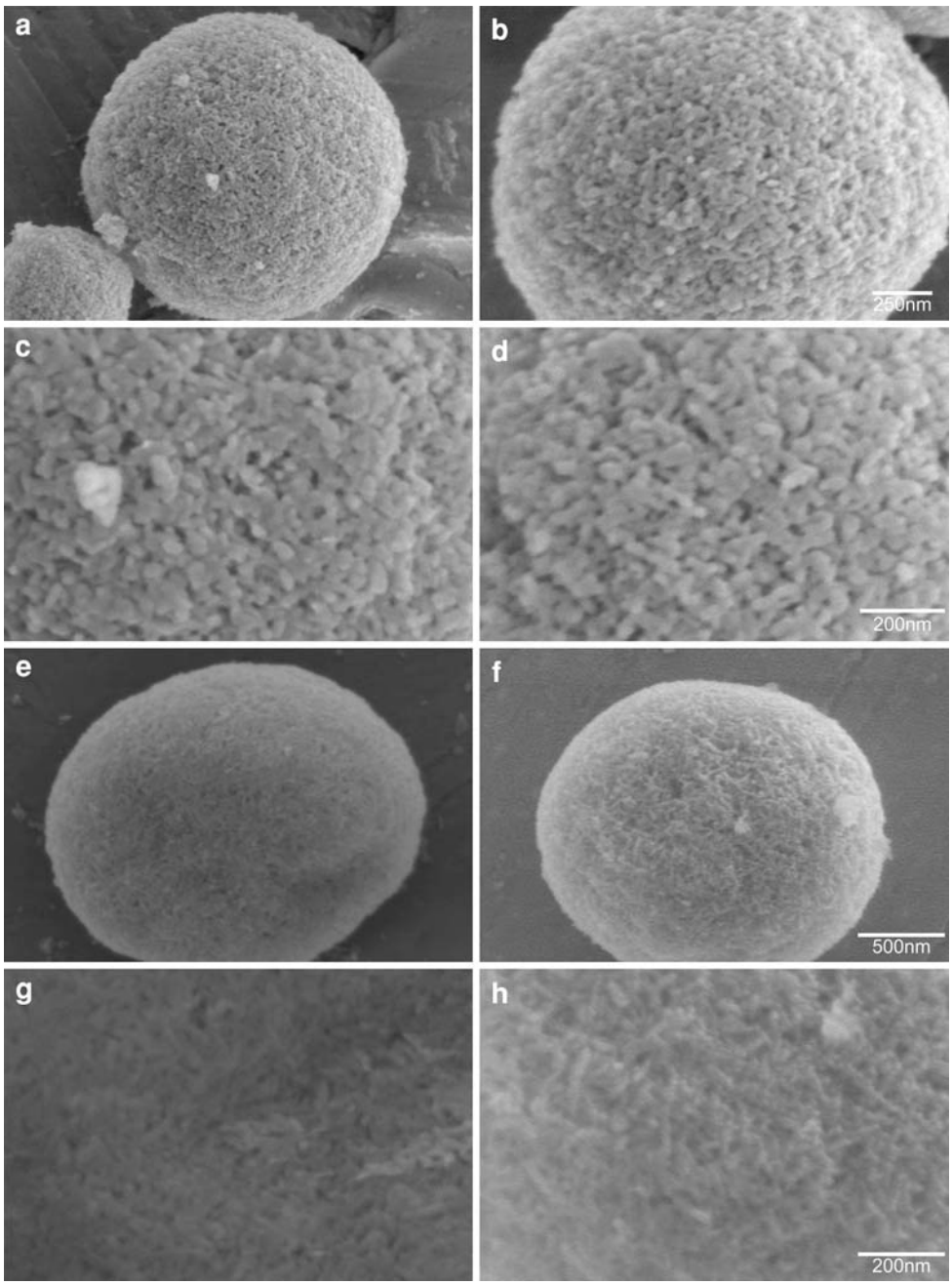

Fig. 10 Scanning electron images of MPs spray dried without trehalose. **a** gel microparticle before heating treatment, **b** gel MP after heat treatment, **c** surface of gel MP before heat treatment, **d** surface of gel MP after heat treatment, **e** colloidal MP before heat treatment, **f** colloidal MP after heat treatment, **g** suface of colloidal MP before heat treatment and **h** surface of colloidal MP after heat treatment

3.3 The effect of initial sugar content of the pore size distribution of material spray dried from hydroxyapatite colloid

The PSDs obtained by BJH analysis of N_2 desorption branch acquired material spray dried with different initial ratios of HA NP colloid to trehalose subsequently heated to 500°C are shown in Fig. 11 and parameterised in Table 3. Comparison of curve a, for the 100% nanoparticle sample, to curve b, for the sample initially containing 95% NP contents shows that the introduction of 5% sugar before heat treatment does not alter the shape of the bottom half of the PSD between 5 and 18 nm. Above 18.5 nm in diameter fewer pores are present in the 95% NP sample compared 100% NP sample. No pores exceeding 30 nm in diameter in the 95% nanoparticle sample. A 36% decrease in pore volume from 0.49 to 0.31 cm^{-3} g^{-1} (Table 4) occurs when the initial NP content is lowered from 100 to 95%. As the initial NP content is reduced to 90%, curve c the PSD shifts to smaller diameters with the peak and maximum pore size decreasing to 16.5 and 28 nm respectively. As the initial NP content reduces from 90 to 50%, curves c through to h Fig. 11, the PSD widens, both maximum pore size and modal pore size increase and the peak height diminishes.

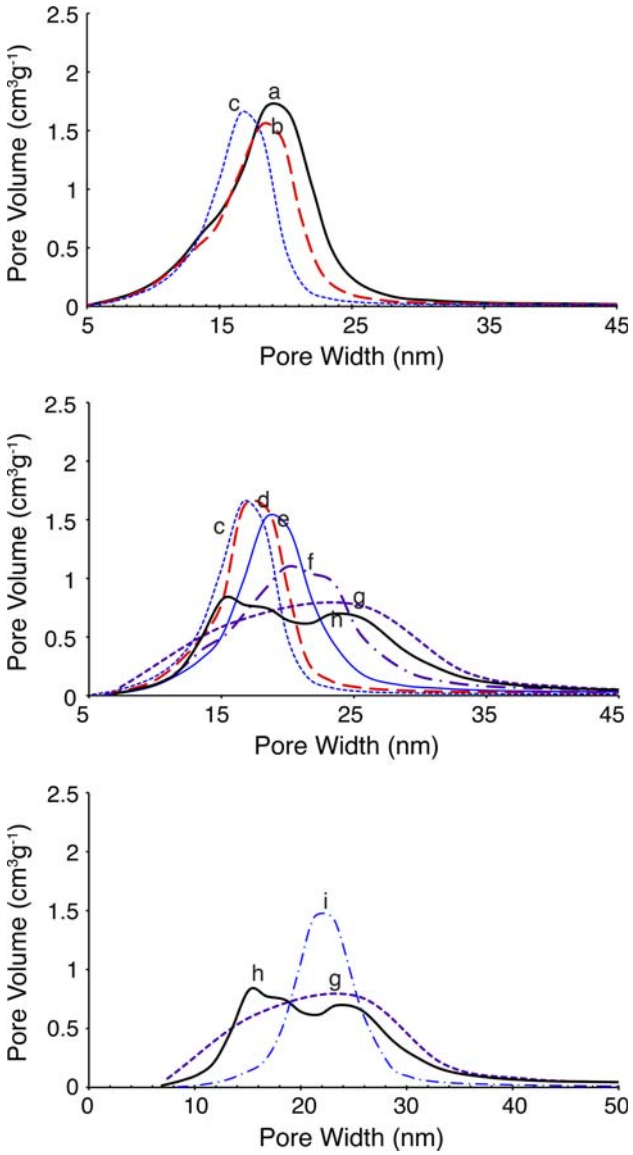

Fig. 11 Pore size distribution obtained by BJH analysis of desorption, branch of N_2 isotherm for MPs spray dried from colloidal NP suspension containing (*a*)100%, (*b*) 95%, (*c*) 90%, (*d*) 80%, (*e*) 70%, (*f*) 60%, (*g*) 55%, (*h*) 50% and (*i*) 40% NPs after heat treatment at 500°C for 3 h

The total pore volume, Table 4, measured by BJH analysis does not vary significantly over this range. The PSD, at 50% initial nanoparticle content becomes bimodal, curve h, with peaks at 15 and 25 nm but reverts to being monomodal with a peak at 21 nm. Between 50 and 40% initial NP content the cumulative pore volume drops significantly from 0.35 to 0.23 cm^{-3} g^{-1}.

PSDs obtained by mercury porosimetry, Fig. 12, Table 5 show similar trend as a function of initial NP content as those obtained by BJH analysis. The PSD sharpens whilst the modal pore size decreases from 16.5 to 15.2 nm as the initial NP content is reduced from 100 to 90%, curves a–c. Lowering initial NP content from 90 to 60%, curves c to f broadens the pore size distribution and increases the modal pore size from 15 to 20 nm. At 60% initial NP content, curve f, the distribution becomes positively skewed beginning to be bimodal at 55% initial NP content. It is clearly biomodal at 50% initial NP content with peaks at 20 and 14 nm but reverts having a single mode around, 19 nm, at 40% initial NP content.

SEM images of the surfaces of MPs originally spray dried with different initial fractions of colloidal HA NPs to trehalose are shown in Fig. 13. Gaps between nanoparticles up 20 nm in width are apparent for preparations without any initial trehalose, Fig. 13a, but most of these spaces are less than this size. These gaps are more evident for MPs spray dried with 95% initial NP content, Fig. 13b. MPs spray dried with 90% initial NP content appear have more tightly packed surfaces with very few inter-nanoparticle separations exceeding 10 nm. As initial NP content is reduced from 90 to 55% the NP packing loosens. At 50%, initial NP content, Fig. 13h, NP separation frequently exceeds 30 nm and sometimes exceeds 100 nm whilst at 40% initial NP content, Fig. 13i, NP packing has tightened.

3.4 The effect of initial sugar content of the pore size distribution of material spray dried from hydroxyapatite gel

Figure 14 shows the PSDs obtained by BJH analysis of desorption for MPs spray dried with various initial ratios of HA gel NPs to trehalose. These distributions are summarised in Table 6. Reducing initial NP content from 100 to 85%, curves a through d Fig. 14 reduces the modal pore size slightly by 2 nm. Pores smaller than the modal pore diameter are gained at the expense of pores greater than the modal diameter without changing the maximum pore size as NP content is decreased over this interval. As the initial NP content is lowered to 80%, curve e, the pore size distribution shifts to larger diameters with the mode increasing to 30 nm and the maximum pore size increasing to 45 nm. Reducing the initial NP content further from 80 to 70%, curves e through to g, returns the PSD back to smaller values dropping the modal pore size from 29 to 19 nm. The PSD broadens and becomes positively skewed, when the initial NP content decreases from 70 to 55%, curves g through j. Over this range the modal pore size increases from 19 to 26 nm as peak height diminishes from 1.60 to 1.35 cm^3 g^{-1} and pore below 15 nm are lost. The PSD is broadest at 50% initial nanoparticle content, curve k, although there is no porosity below 15 nm at this initial NP content. The distribution becomes bimodal at 40% initial NP content, curve j, with a sharp maximum at 26 nm and a diffuse maximum at 50 nm but reverts to being monomodal at 30% initial NP content.

Table 3 Parameters ascribed to the pore size distributions obtained by BJH analysis of the desorption branch of the gas-isotherm acquired after heat of material spray dried with different initial ratios of hydroxyapatite nanoparticle colloid to trehalose shown in Fig. 11

Nanoparticle content (%)	Curve in figure	Minimum (nm)	Maximum (nm)	Range (nm)	Peak (nm)	Width at half height (nm)	Peak height ($cm^3\ g^{-1}$)
100	a	5	35	30	19.5	7	1.70
95	b	5	30	25	18.5	6	1.55
90	c	5	28	23	16.5	5	1.65
80	d	5	30	25	17.5	5.2	1.65
70	e	6	35	29	19	6	1.53
60	f	5	41	36	21.7	9.8	1.11
55	g	6	45	39	24	19	0.80
50	h	6	45	39	25 (15)	16	0.72
40	i	10	36	26	21	9	1.55

Table 4 Properties determined by analysis of N_2 sorption acquired for material spray dried with different initial ratios of hydroxyapatite nanoparticle colloid to trehalose after heating to 500°C for 3 h

Nanoparticle content (%)	Micropore area ($m^2\ g^{-1}$)	Micropore area (%)	External surface area ($m^2\ g^{-1}$)	Total surface area (BET) ($m^2\ g^{-1}$)	Micropore volume ($\times 10^{-3}\ cm^3\ g^{-1}$)	Micropore volume (%)	Cumulative pore volume (BJH) ($cm^3\ g^{-1}$)
100	9.9	13.5	63.3	73.2	4.48	0.9	0.49
95	3.9	6.8	53.6	57.5	1.08	0.3	0.31
90	3.6	6.7	49.5	53.1	0.98	0.3	0.35
80	7.3	14.3	43.8	51.2	3.41	1.1	0.31
70	5.7	12.6	39.4	45.2	2.65	0.9	0.30
60	4.1	8.6	43.1	47.2	1.33	0.4	0.30
55	9.0	18.8	39.0	48.1	4.21	1.2	0.35
50	11.0	21.1	41.0	52.0	5.13	1.4	0.35
40	*	*	26.9	26.1	*	*	0.23

* Cannot be determined by T-plot analysis

Total pore volume, Table 7, measured by BJH analysis decreases from 0.40 $cm^3\ g^{-1}$ at 100% initial NP content to 0.35 $cm^3\ g^{-1}$ at 80% initial NP content. Then it raises to its greatest value 0.44 $cm^3\ g^{-1}$, at 55% initial NP content and falls to its least value, 0.34 $cm^3\ g^{-1}$, at 50% initial NP content. Changes in pore volume observed using mercury porosimetry, Table 8 are barely significant but show a similar trend.

Figure 15 shows the PSD obtained by mercury porosimetry for microparticles spray dried with various initial ratios of HA gel NPs to trehalose. These distributions summarised in Table 8, show a similar tend with increasing trehalose content as those obtained by BJH analysis of N_2 desorption. Lowering NP content from 100 to 85%, curves a to d, causes little alteration in the PSD apart from a slight alteration in the height of the maxima. Decreasing the initial NP content from 85 to 75%, curves d, e and f, increases the modal pore size from 19 to 22 nm leaving the breadth of the distribution unchanged. As the initial NP content drops from 75 to 70%, curves f and g the peak pore size decreases from 22 to 17 nm and the peak height diminishes leaving the breadth of the PSD unchanged. Between 70 and 50 the distribution broadens and the peak value shifts from 17 to 43 nm. At 55, 50 and 40% initial NP content the distribution is bimodal but the distribution reverts to having a single peak at 30%.

SEM images of heat treated MPs originally spray dried with different fractions of HA gel to trehalose are shown in Fig. 16. NP packing loosens as initial NP content is decreased from 100 to 90% Fig. 16a–c but appears more compact at 85% initial NP content. Decreasing the NP content below 85%, Fig. 16c–m increases the space between NPs. Gaps as large as 50 nm existing between NPs at 40% initial NP content whilst at 30% initial NP content, Fig. 16m, NP packing of reverts to a more compact configuration.

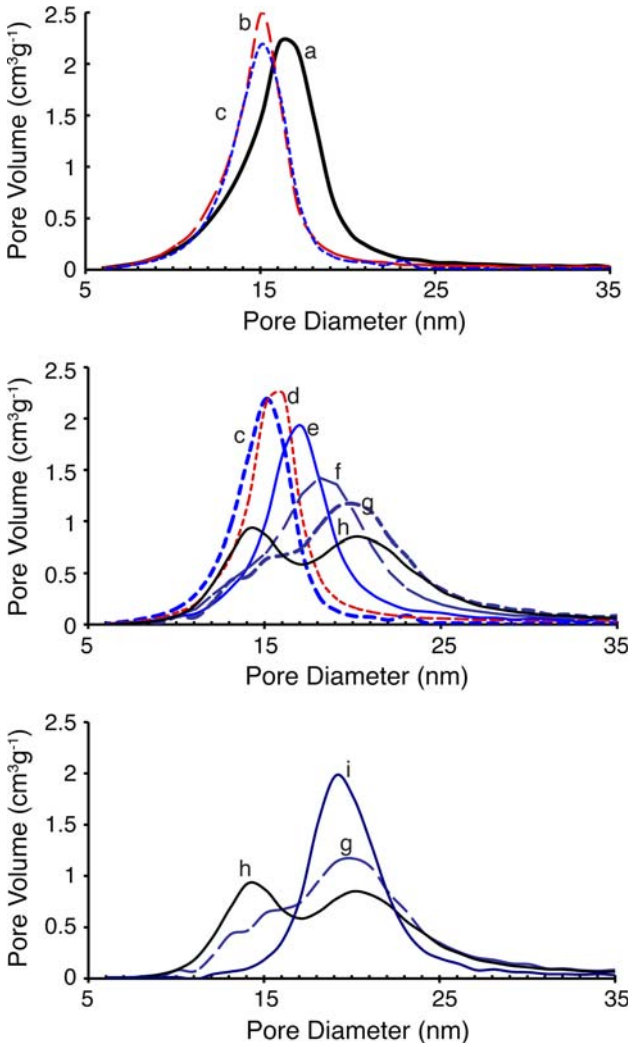

Fig. 12 Pore size distribution determined by mercury porosimetry for MPs spray dried from colloidal NP suspensions containing (*a*) 100%, (*b*) 95%, (*c*) 90%, (*d*) 80%, (*e*) 70%, (*f*) 60%, (*g*) 55%, (*h*) 50% and (*i*) 40% NPs after heat treatment at 500°C for 3 h

4 Discussion

BJH analysis of pore size using the desorption branch the of N_2 isotherm is justified when micropore volume is small and the N_2 isotherm is of type IV accompanied by a type H1 hysteresis loop, according to IUPAC classification [16]. For MP preparations spray dried without trehalose and all those where the sugar component has been eliminated this was the case. The space between NPs is a highly interconnected. During desorption, larger pores inside MPs may need to empty of N_2 though a network of smaller pores connecting them to the MP's surface. BJH analysis of desorption is, therefore, likely to predict a smaller PSD than is actually present. Indeed, BJH analysis of adsorption, less prone to network effects and more likely to reflect real pore size [16], gives considerably larger pore sizes and broader PSD for MP material. Unfortunately, the pressure transducer of any gas analyser has finite accuracy. This limits data point separation, particularly at larger pore sizes as pore size is inversely proportional to the relative pressure according to the Kelvin equation used for BJH analysis. For the Tristar 3000, used here this means in practice that only two or three data points can be obtained between 50 and 100 nm limiting the precision to which the PSD can be plotted. For this reason, the desorption branch of the N_2 gas isotherm was used for comparison of the PSDs. They are also reported as they are in reasonable agreement with those obtained by mercury intrusion. Good agreement with mercury intrusion is probable as mercury is likely to fill during intrusion though smaller pores at surface of the MP into larger pores within its interior. PSDs obtained from extrusion data are rejected overestimates because mercury will preferentially empty through a small subpopulation of larger pores [17]. Analysis of mercury extrusion (not reported) predicted considerably larger pores than those

Table 5 Parameters describing the pore size distributions obtained by mercury porosimetry (shown in Fig. 12) of material spray dried with different initial ratios of hydroxyapatite nanoparticle colloid to trehalose after heat treatment

Nanoparticle content (%)	Curve in figure	Minimum (nm)	Maximum (nm)	Range (nm)	Peak nm	Width at half height (nm)	Height ($cm^3\ g^{-1}$)	Cumulative ($cm^3\ g^{-1}$)	Pore area ($m^2\ g^{-1}$)
100	a	6	30	24	16.5	4.5	2.25	0.34	89.10
95	b	6	23	17	15	3	2.5	0.31	84.82
90	c	6	20	14	15.2	3.6	2.2	0.28	77.14
80	d	6	23	17	16	4	2.3	0.30	75.70
70	e	6	30	24	17	4	1.95	0.28	65.68
60	f	6	30	24	18	5.5	1.4	0.31	68.75
55	g	6	35	29	20	8	1.15	0.29	62.56
50	h	6	35	29	20 (14)	8	0.8 (0.95)	0.27	63.37
40	i	12	30	18	19	4	2	0.25	49.39

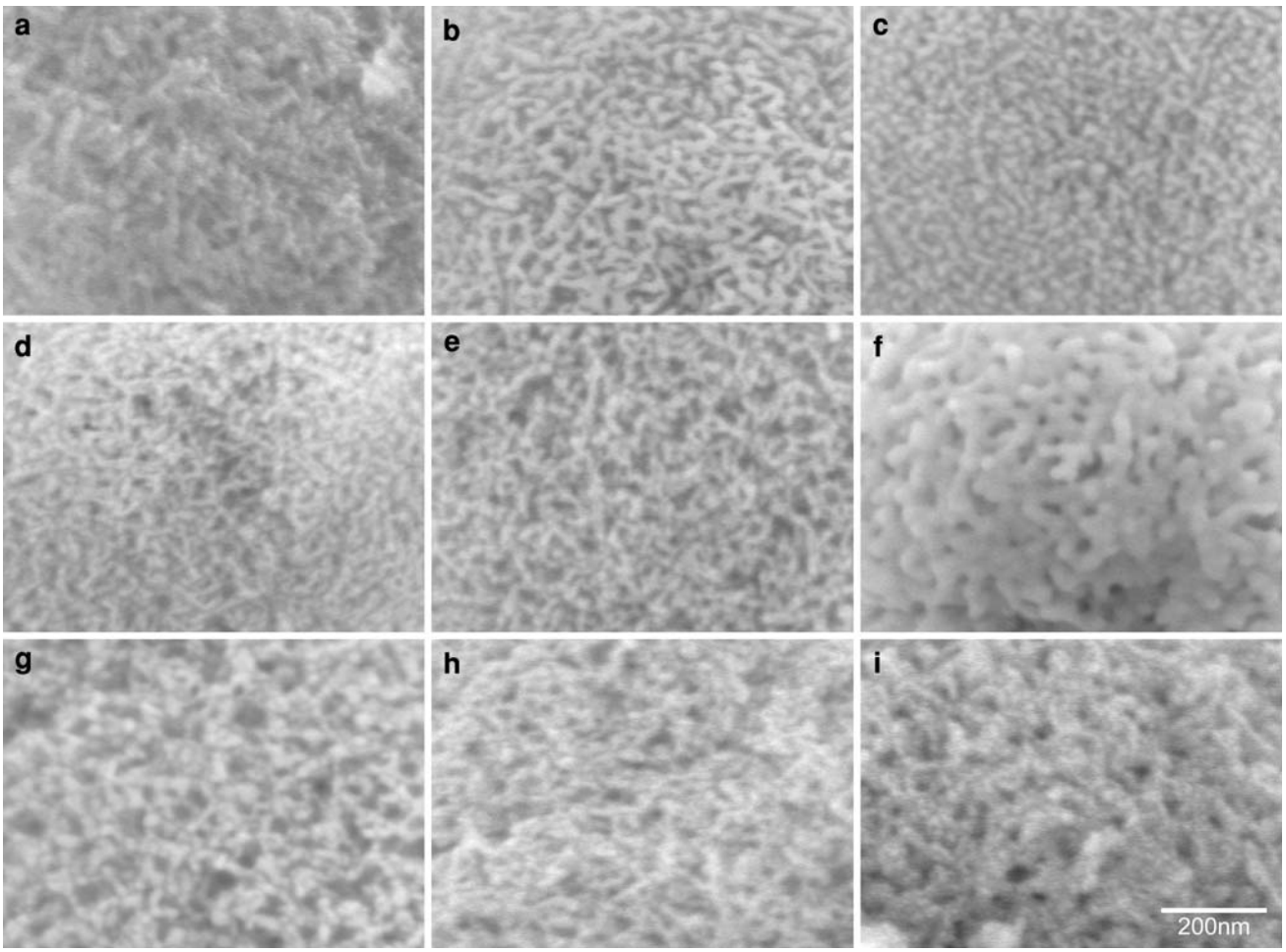

Fig. 13 Image of surface of spray dried colloid MP containing **a** 100%, **b** 95%, **c** 90%, **d** 80%, **e** 70%, **f** 60%, **g** 55%, **h** 50% and **i** 40% NPs after heat treatment obtained by scanning electron microscopy

obtained by BJH adsorption. Detailed analysis of intrusion–extrusion hysteresis can yield information about the interconnectivity of pore space if an appropriate model is applied [18] and should be considered for future studies of meso-porosity in material spray dried from nanoparticles.

Modal pore diameter (Table 1) is comparable with NP width (Fig. 1) for both colloid and gel preparations spray dried without sugar. It is slightly less than modal NP width (20 nm) according to BJH analysis of desorption and mercury intrusion and slightly greater than modal nanoparticle width according to BJH analysis of adsorption. Modal pore size is greater for spray dried gel than for spray dried colloid according to all measures of pore size. Neighbouring NP may, prefer to pack in a manner disfavouring short axis alignment and favouring long axis alignment especially when there surface change distribution is modified with citrate Citrate binds preferentially to calcium and assembles onto crystalline hydroxyapatite facets in an organised manner [19] and the resulting non-uniform distribution of charge may favour certain ways of NP packing. This may explain why in the absence of the sugar component (and before heat treatment) colloid NPs pack more tightly during the spray drying process, with 25% less space between NPs, than gel NPs.

As the aim of this investigation was to determine the influence the sugar glass component has on the separation of NPs temperatures able to melt and fuse nanoparticles were avoided. Densification and changes in NP morphology might be anticipated at temperatures well below 1100°C, the temperature usually used for sintering HA bioceramics in the bulk, because large surface energy associated NPs contributes to fusion. NPs at the MP surface appear unaltered by heating to 500°C for 5 h, the lowest temperature at which trehalose is eliminated. NPs are more loosely packed at the surface of MPs spray dried from colloidal HA alone after heat treatment which may relate to the 20 to 25% increase in inter-nanoparticle volume after heat treatment. Packing of NPs at the surface of MPs spray

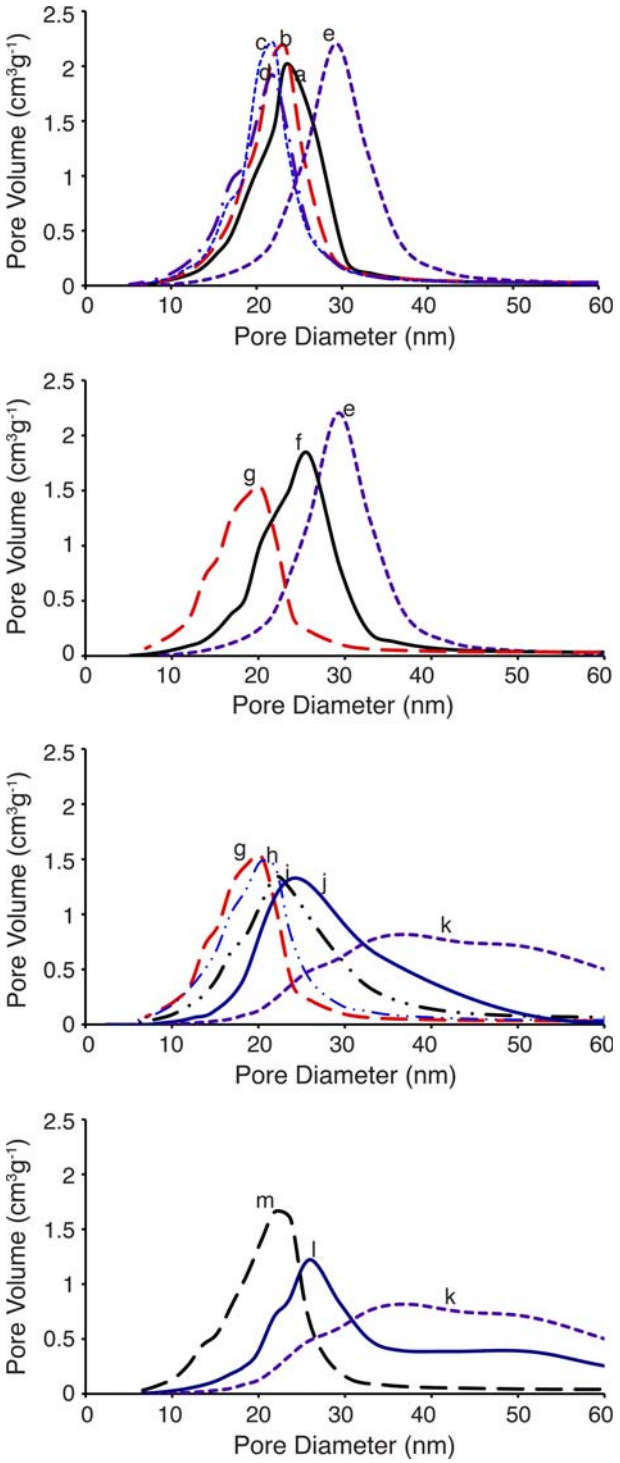

Fig. 14 Pore size distribution obtained by BJH analysis of desorption, branch of N_2 isotherm for MP spray dried from NP gel containing *a* 100%, *b* 95%, *c* 90%, *d* 85%, *e* 80%, *f* 75%, *g* 70%, *h* 65%, *i* 60%, *j* 55%, *k* 50%, *l* 40% and *m* 30% nanoparticles after heat treatment at 500°C for 3 h

dried from gel appears unaltered by heat treatment as does the internal volume measured by both mercury and gas techniques. Heating treatment of material spray dried

Table 6 Parameters describing the pore size distributions obtained by BJH analysis of the desorption branch of the gas-isotherm acquired after heat treatment of material spray dried with different ratios of hydroxyapatite nanoparticle gel to trehalose shown in Fig. 14

Nanoparticle content (%)	Curve in figure	Minimum (nm)	Maximum (nm)	Range (nm)	Peak (nm)	Width at half height (nm)	Peak height ($cm^3\ g^{-1}$)
100	a	6	42	36	24	8	2.00
95	b	6	40	34	24	8	2.20
90	c	6	40	34	22	6	2.25
85	d	5	40	35	22	7	1.95
80	e	10	50	40	29	8	2.25
75	f	5	40	35	26	9	1.85
70	g	5	34	29	19	10	1.60
65	h	5	40	35	20	9	1.50
60	i	5	50	45	22	12	1.40
55	j	8	58	50	24	34	1.35
50	k	5	80	60	50(36)	40	0.80 (0.75)
40	l	5	80	60	50(26)	38(10)	0.40(1.25)
30	m	5	36	60	22	9	1.70

Table 7 Properties determined by analysis of N_2 sorption acquired for material spray dried with different initial ratios of hydroxyapatite nanoparticle gel to trehalose after heating to 500°C for 3 h

Nanoparticle content (%)	Micropore area ($m^2\ g^{-1}$)	Micropore area (%)	External surface area ($m^2\ g^{-1}$)	Total surface area (BET) ($m^2\ g^{-1}$)	Micropore volume ($\times 10^{-3}\ cm^3\ g^{-1}$)	Micropore volume (%)	Cumulative pore volume (BJH) ($cm^3\ g^{-1}$)
100	3.61	6.93	48.50	52.10	1.014	0.25	0.40
95	*	*	52.71	52.71	*	*	0.38
90	*	*	53.52	53.52	*	*	0.36
85	*	*	58.81	58.81	*	*	0.39
80	*	*	36.78	36.78	*	*	0.35
75	2.04	4.22	46.35	48.40	0.244	0.06	0.38
70	2.90	4.30	64.52	67.42	0.38	0.09	0.41
65	*	*	63.29	64.78	*	*	0.39
60	*	*	50.63	51.54	*	*	0.39
55	7.04	14.67	40.92	47.95	3.003	0.68	0.44
50	3.37	10.60	28.43	31.80	1.172	0.34	0.34
40	0.00	*	34.85	34.85	*	*	0.36
30	3.95	6.21	59.72	63.67	0.988	0.24	0.42

* Cannot be determined by T-plot analysis

Table 8 Parameters describing the pore size distributions obtained by mercury porosimetry (shown in Fig. 15) of material spray dried with different ratios of hydroxyapatite nanoparticle gel to trehalose after heat treatment

Nanoparticle Content (%)		Minimum (nm)	Maximum (nm)	Range (nm)	Peak (nm)	Width at half height (nm)	Height $cm^3\ g^{-1}$	Cumulative $cm^3 g^{-1}$	Pore area ($m^2\ g^{-1}$)
100	a	6	30	24	19	3.5	2.95	0.38	86.65
95	b	6	30	24	19	3.5	3.5	0.40	86.37
90	c	6	32	26	18.8	3	3.75	0.39	87.92
85	d	6	32	26	19	4	2.75	0.40	89.59
80	e	7	32	25	20	4.2	3	0.39	81.40
75	f	8	35	27	22	4	3	0.39	77.08
70	g	6	30	24	17	4	2.3	0.38	95.50
65	h	5	34	29	18	5	2.25	0.41	94.02
60	i	9	45	36	20	9	1.75	0.41	81.78
55	j	10	48	38	26 (18)	26	1.1 (1)	0.42	74.32
50	k	15	65	50	43 (28)	20 (10)	1.2 (0.8)	0.38	46.08
40	l	6	70	64	35 (19)	24 (5)	0.5 (1.35)	0.41	73.32
30	m	6	30	24	19	4.5	2.4	0.39	89.81

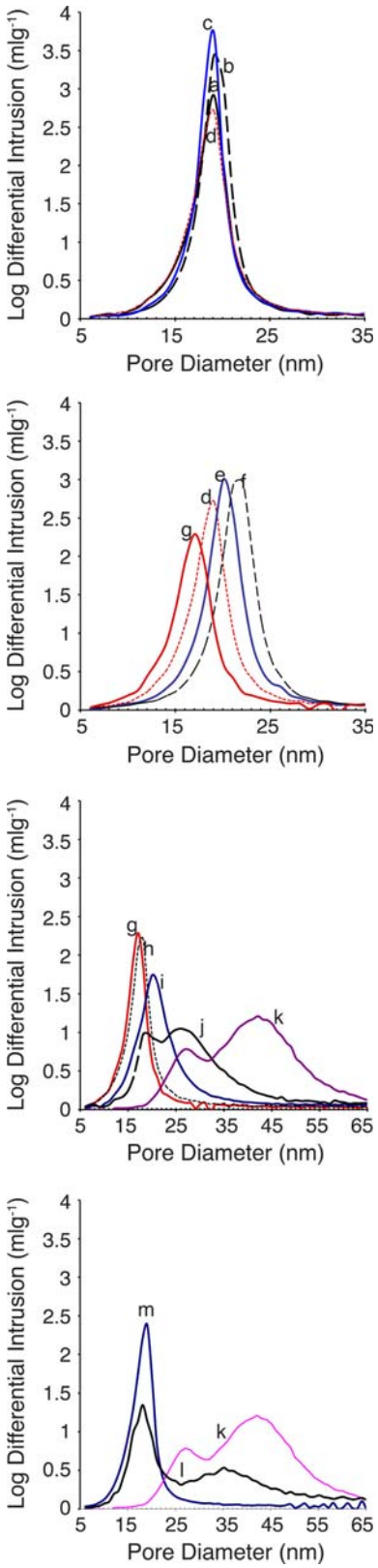

Fig. 15 Pore size distribution determined by mercury porosimetry for microparticles spray dried from nanoparticle gel containing *a* 100%, *b* 95%, *c* 90%, *d* 85%, *e* 80%, *f* 75%, *g* 70%, *h* 65%, *i* 60%, *j* 55%, *k* 50%, *l* 40% and *m* 30% after heat treatment at 500°C for 3 h

solely from HA NPs shifts the PSDs to larger values. Changes in NP dimensions, likely to explain this gain of larger pores at the expense loss of smaller ones, may result from a thin 1–2 nm of hydrated amorphous calcium phosphate layer, recently reported [20] on the surface of HA precipitates transforming into HA when heated above 300°C. As these transformation may occur if the sugar glass component is present or absent preparations spray dried without sugar where subjected to heat treatment and used as controls when exploring the influence of the sugar fraction on the porosity.

Material spray dried from HA gel has significant micropore area whereas, material spray dried from colloid has no micropore area. Microporosity may arise due to the outer layer of ACP or poorly crystalline apatite on the surface of the nanoparticles and may enhance their ability to trap antigen. This layer may form during spray drying if solution in which the NP feed stock is suspended contains free calcium and phosphate that will crash out of solution as the aqueous solvent evaporates in the drying process. This layer has been suggested to be responsible for irreversible adhesions formed between HA NPs on drying [21], and may explain why HA NPs spray dried without sugar form cohesive MPs. MPs consisting solely of this type calcium phosphate have recently been made by spray drying acidic solutions saturated with respect to calcium and phosphate [22].

4.1 The influence of intial sugar content of the pore size distributions obtained after elimination of the sugar glass component

After heat treatment PSDs for material spray dried with up to 20% trehalose and for gel preparations spray with gel up to 15% trehalose for colloid, closely resemble those for control preparations initially spray dried without sugar. A possible explanation for this is that spray drying with small fractions of sugar may just fill voids between abutting nanoparticles with sugar and not generate extra inter-nanoparticle space by increasing nanoparticle separation. There is, however, small shift in the pore size distribution to slightly lower values for MPs originally containing small sugar relative to that of control spray dried without sugar. This suggests that whilst assembling into MPs, NPs become coated with a thin trehalose film that when eliminated by combustion causes the interconnected network of NPs to shrink, as illustrated by Fig. 17, creating smaller pores at the expense of larger ones. The creation of nanometer-sized trehalose containing volumes small enough to entrap antigen upon spray drying with small amounts of sugar is suggested by this shift.

Material spray dried with colloidal HA exhibits a broadening and shift in pore size distribution to larger

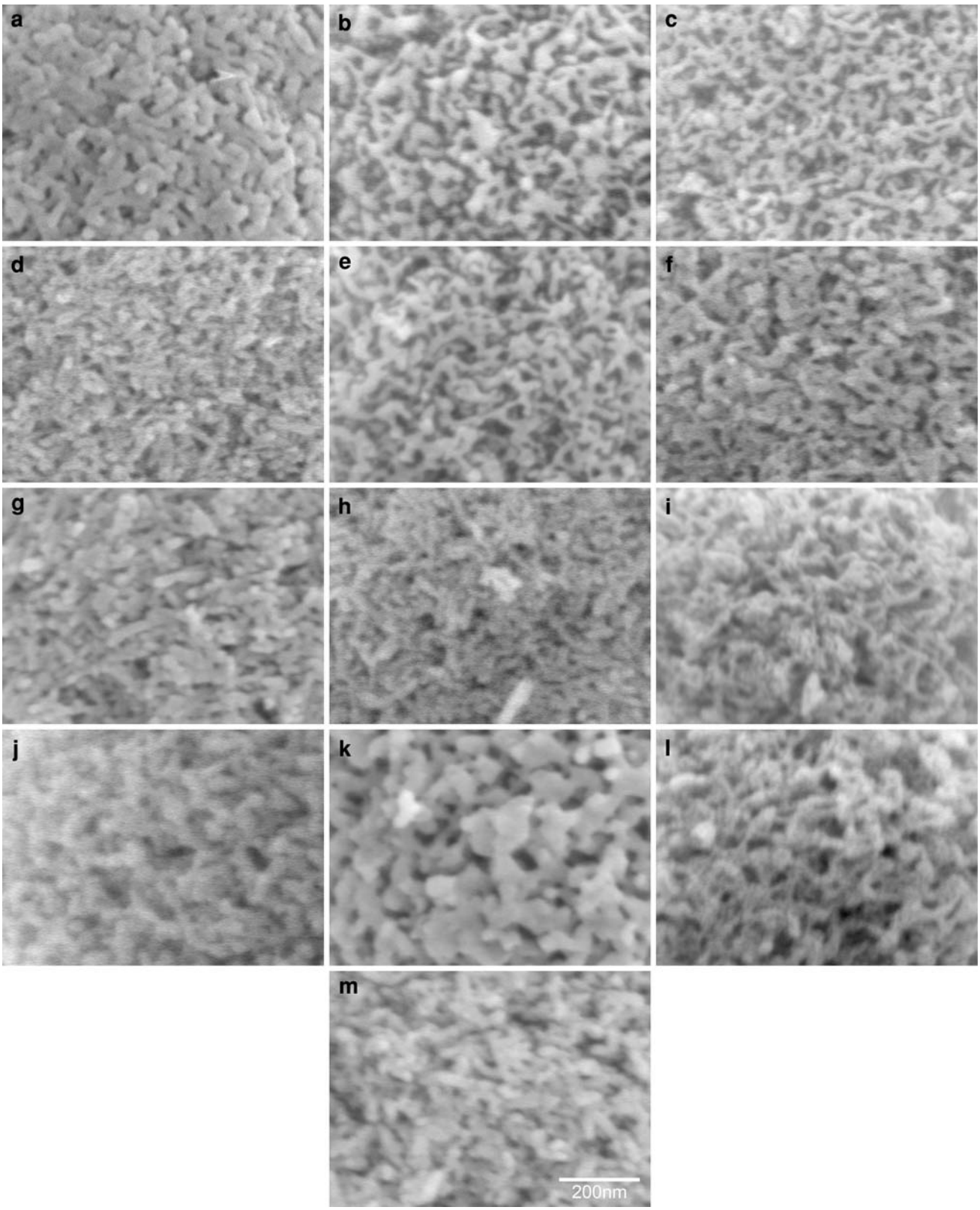

Fig. 16 Image of surface of spray dried gel microparticles containing **a** 100%, **b** 95%, **c** 90%, **d** 85%, **e** 80%, **f** 75%, **g** 70%, **h** 65%, **i** 60%, **j** 55%, **k** 50%, **l** 40% and **m** 30% after heat treatment at 500°C for 3 h

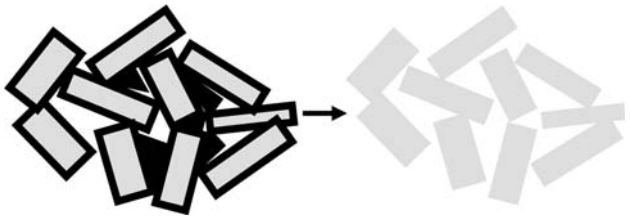

Fig. 17 2D schematic diagram illustrating the probably effect the elimination of trehalose likely only to be located between nanoparticles and as a film covering their surface suggested at low sugar content

values as the initial NP content is reduced from 80 to 50%, which also occurs for material spray dried from gel as the initial nanoparticle content is reduced from 70 to 40%. These observations suggest a point reached is reached where the void space between abutting NPs is full and to accommodate more sugar the NP network has to become progressively more open. This more open structure may provide an easy route for antigens to leave the confines of the MP and foreshorten their release.

The space contained between NP, measured by both mercury and BJH analysis for colloidal material changes little with from 80 to 60% initial NP content but shows a slight increase at 55% initial NP content. Partial collapse on heat treatment may be occurring as increase in the total volume of these preparations might be expected. Burning away the trehalose may lock the NP network into a more open configuration even if structural collapse occurs as sugar melts before it burns. The pore size distributions obtained by combustion of the sugar glass component may under estimate the space separating NP inside MPs containing sugar.

PSDs for material spray dried with large trehalose fractions, 40% for colloid and 30% for gel, resemble those for control material initially spray dried without trehalose. NP are perhaps initially too sparse and to form an interconnected network in these preparations and when the sugar component melts, individual NPs are likely to undergo Brownian motion that is initially unimpeded by neighbouring NPs. As slow heating rate for this study 5°C min^{-1}, NPs have ample time to reorganise before the sugar is incinerated. So instead of locking into an open configuration with larger pores the NPs compact. The fall in cumulative pore volume, seen by BJH analysis between 55 and 40% initial NP content for gel derived material and between 50 and 40% initial for colloid derived material is evidence of compaction. Compaction also suggested by SEM observations. MP spray dried from colloid show loosest NP packing at 50% NP content but much tighter NP packing at 40% NP content. MPs spray dried from gel show loosest NP packing at 40% initial NP content but much tighter NP packing at 30% initial NP content. PSDs

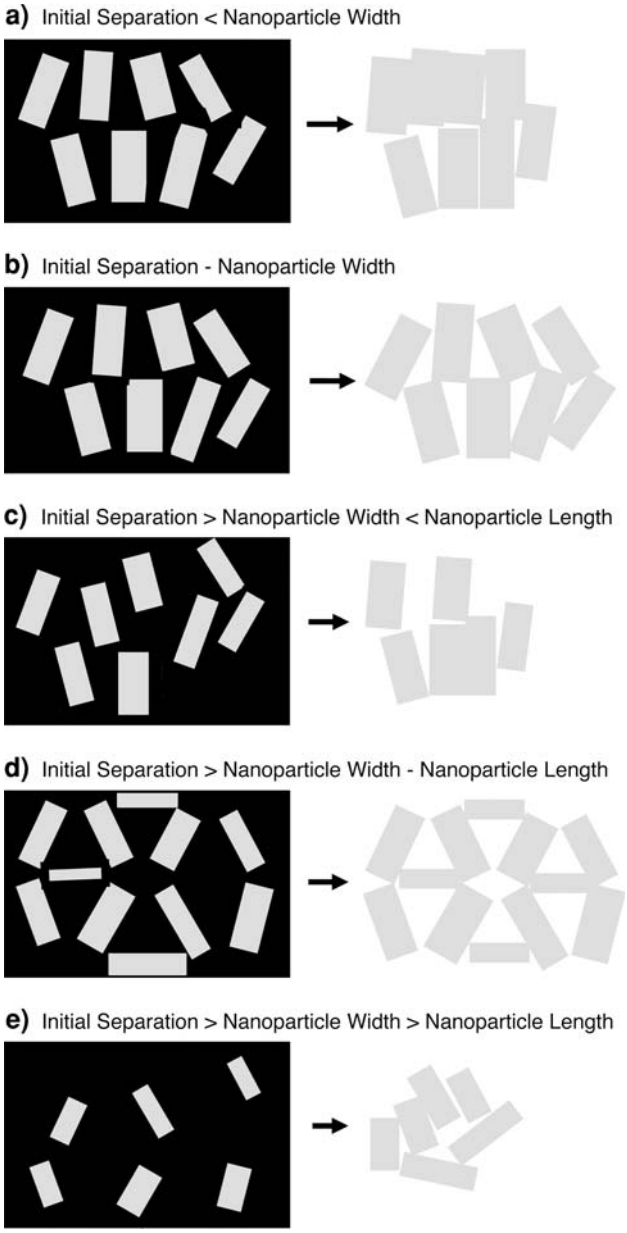

Fig. 18 2D schematic diagram illustrating the initial nanoparticle separation and its proposed effect the resultant NP network structure after elimination of the trehalose where **a** initial NP separation is less than NP width, **b** where intial NP separation is comparable with NP width, **c** initial NP separation exceeds nanoparticle width but is less than NP length, **d** NP separation is comparable to NP and **e** where NP exceeds NP length

obtained for some preparations with between 55 and 40% NP content are biomodal. These MPs are likely to contain regions both sparsely and more densely populated by NPs.

For material spray dried from gel there is an abrupt shift in pore size distribution to higher values as the initial NP content is decreased from 85 and 80% and an abrupt shift back to smaller values as the initial NP content is decreased to 70%. This trend, not mirrored for colloid derived

material and may be a consequence of the looser NP packing of gel NP which can be explained as follows with the help of Fig. 18. Below 85% initial nanoparticle content, Fig. 18a, the increased NP separation due to the initial presence of the sugar component is unlikely to exceed the NP width. The initial close proximity of NPs with their neighbours highly restricts NP translation and rotational motion when the trehalose is molten and the network of NPs collapses back into the dense configuration of the control material when the trehalose is eliminated. Near 80% initial NP content NP separation approximates to the NP width and NPs potentially have room to slide past each but lack rotational freedom when the sugar is molten. The resultant interpenetrating arrangement of the NPs means they lock into an open structure rather than adopting the denser configuration of the control material. At 70% initial NP content, the NP separation exceeds the width of most NPs but length very few NPs. They therefore, have more but restricted rotational and translational freedom but this is enough freedom for the NPs to adopt a denser network configuration of the control on melting. Below 70% initial NP content, the space between NP begins to exceed shorter NP lengths but not longer ones in the NP population. In the molten trehalose shorter nanoparticles may have full translational and rotational freedom about all axes whereas the movement of longer NPs is restricted perhaps impinging on each other and forming their own interconnected network. As the trehalose melts, shorter NPs will intersperse between the longer ones and as a consequence when the assembly of NPs jam into a more open structure when the trehalose is eliminated by combustion. Below 40% NP content the initial NP separation may exceed the length of most of the population of NPs. All NPs will have full rotational and translational freedom when the trehalose is in a molten state and the NP network will collapse back to that of the control sample when the trehalose is eliminated. Microparticles with this sugar content immediately disintegrate into their component nanoparticles on contact with water.

Mesoporous materials based on silica, have recently received renewed interest as drug carriers because mesopore size, mesopore volume and total surface area can potentially be tailored to influence macromolecular release and absorption [23]. Silica MPs with controllable interconnected mesoscale channels demonstrate pore size-selective adsorption for proteins over the molecular weight range 20–100 KDa [24]. Here pore diameters of HA MPs have been tailored over the same range by spray drying with a glass forming sugar auxiliary eliminated subsequently eliminated by combustion. These are of potentially greater use for biomacromolecular separation as the ability of apatite to physicochemically bind particular proteins can also be tailored. Since proteins can be immobilised and stabilised within the microparticle interior by spray drying the ratio of sugar to hydroxyapatite nanoparticles can be used to manipulate the rate of release which will depend on the pore diameter relative to the effective protein diameter.

5 Conclusions

Spray drying with colloidal hydroxyapatite nanoparticles produces denser microparticles containing smaller pores than microparticles spray dried from hydroxyapatite nanoparticle gel. As increasingly larger fractions of trehalose are introduced to the spray drying process nanoparticle separation progressively increases which causes the resultant interconnected network of nanoparticles to adopt conformations containing increasingly larger mesopores when the trehalose is eliminated by combustion. An initial trehalose content is reached, 40% for spray dried gel and 50% for spray dried colloid, where nanoparticles are too dispersed to form a continuous network and combustion of the trehalose causes the MP's pore structure to collapse.

Acknowledgments This work was funded by a DTI grant (CHBS/004/00063C) held jointly by J. N. Skepper at the University of Cambridge and Cambridge Biostability Ltd. We would like to thank Wayne Hough for his assistance in running samples for Mercury Porosimetry and Dr. Serena Best for access to equipment run within her laboratory.

References

1. Motskin M, Wright DM, Muller K, Kyle N, Gard TG, Porter AE, et al. Hydroxyapatite nano and microparticles: correlation of particle properties with cytotoxicity and biostability. Biomaterials. 2009;30:3307–17.
2. Wright DM, Rickard JJ, Kyle N, Gard T, Dobberstein H, Motskin M, et al. The use of dual beam ESEM FIB to reveal the internal ultrastructure of hydroxyapatite nanoparticle-sugar-glass composites. J Mater Sci Med. 2009;20:203–14.
3. Midgley PA, Dunin-Borkowski RE. Electron tomography and holography in materials science. Nat Mater. 2009;8:271–80.
4. Joyner LG, Barrett EP, Skold R. The determination of pore volume and area distribution in porous substances. Comparison between nitrogen isotherm and mercury porosimeter methods. J Am Chem Soc. 1951;73:3155–8.
5. Washburn EW. The dynamics of capillary flow. Phys Rev. 1921;17:273–83.
6. Rouquerol J, Avnir D, Fairbridge CW, Everett DH, Haynes JH, PErnicone N, et al. Recommendations for the characterization ofporous solids. Pure Appl Chem. 1994;66:1739–58.
7. Diamond S. A re-evaluation of hardened cement paste microstructure based on backscatter SEM investigations. Cem Concr Res. 2000;30:1517–25.
8. Tuan Ho S, Hutmacher DW. A comparison of micro CT with other techniques used in the characterization of scaffolds. Biomaterials. 2006;27:1362–76.
9. Padilla S, Román J, Vallet-Regí M. Synthesis of porous hydroxyapatites by combination of gelcasting and foams burn out methods. J Mater Sci Med. 2002;13:1193–7.

10. Kaneko K. Determination of pore size and pore size distribution 1. Adsorbents and catalysts. J Membr Sci. 1994;96:59–89.
11. Webb PA, Orr C. Analytical methods in fine particle technology, Micromeritics; 1997.
12. Brunauer S, Emmett PH, Teller E. Adsorption of gases in multimolecular layers. J Am Chem Soc. 1938;60:309–19.
13. Barrett EP, Joyner LG, Halenda PP. J Am Chem Soc. The determination of pore volume and area distribution in porous substances. I. Computations from nitrogen isotherms. 1951; 73:373–80.
14. Cracknell RF, Gubbins KE, Maddox M, Nicholson D. Behavior in well-characterized porous materials. Acc Chem Res. 1995; 28:281–8.
15. Kumta PN, Sfeir C, Lee DH, Olton D, Choi D. Nanostructured calcium phosphates for biomedical applications: novel synthesis and characterization. Acta Biomater. 2005;1:65–83.
16. Groen JC, Peffer LAA, Perez-Ramirez J. Pore size determination in modified micro- and mesoporous materials. Pitfalls and limitations in gas adsorption data analysis. Microporous Mesoporous Mater. 2003;60:1–17.
17. Ciftcioglu M, Smith DM, Ross SB. Mercury porosimetry of ordered sphere compacts: Investigation of intrusion and extrusion pore size distributions. Powder Technol. 1988;55:193–205.
18. Portsmouth RL, Gladden LF. Determination of pore connectivity by mercury porosimetry. Chem Eng Sci. 1991;46:3023–36.
19. Jiang W, Pan H, Cai Y, Tao J, Liu P, Xu X, et al. Atomic force microscopy reveals hydroxyapatite-citrate interfacial structure at the atomic level. Langmuir. 2008;24:12446–51.
20. Bertinetti L, Tampieri A, Landi E, Ducati C, Midgley PA, Coluccia S, et al. Surface structure, hydration, and cationic sites of nanohydroxyapatite: UHR-TEM, IR, and microgravimetric studies. J Phys Chem C. 2007;111(10):4027–35.
21. Drouet C, Bosc F, Banu M, Largeot C, Combes C, Dechambre G, et al. Nanocrystalline apatites: from powders to biomaterials. Powder Technol. 2009;190(1–2):118–22.
22. Chow LC, Sun LM, Hockey B. Properties of nanostructured hydroxyapatite prepared by a spray drying technique. J Res Natl Inst Stand Technol. 2004;109(6):543–51.
23. Colilla M, Manzano M, Vallet-Regi M. Recent advances in ceramic implants as drug delivery systems for biomedical applications. Int J Nanomed. 2008;3:403–14.
24. CHen LH, Zhu GS, Zhang DL, Zhao H, Guo MY, Wei SB, et al. Novel mesoporous silica spheres with ultra-large pore sizes and their application in protein separation. J Mater Chem. 2009; 19(14):2013–7.